

1 **Unleashing the Potential of Geostationary Satellite Observations in Air**  
2 **Quality Forecasting Through Artificial Intelligence Techniques**

3 Chengxin Zhang<sup>1</sup>, Xinhan Niu<sup>1</sup>, Hongyu Wu<sup>2</sup>, Zhipeng Ding<sup>2</sup>, Ka Lok Chan<sup>3</sup>, Jhoon Kim<sup>4</sup>,  
4 Thomas Wagner<sup>5</sup>, Cheng Liu<sup>1,6,7\*</sup>

5 <sup>1</sup>Department of Precision Machinery and Precision Instrumentation, University of Science and  
6 Technology of China, Hefei, 230026, China

7 <sup>2</sup>School of Environmental Science and Optoelectronic Technology, University of Science and  
8 Technology of China, Hefei, 230026, China

9 <sup>3</sup>Rutherford Appleton Laboratory Space, Harwell Oxford, United Kingdom

10 <sup>4</sup>Department of Atmospheric Sciences, Yonsei University, Seoul, Republic of Korea

11 <sup>5</sup>Satellite Remote Sensing Group, Max Planck Institute for Chemistry, Mainz, Germany

12 <sup>6</sup>Key Laboratory of Environmental Optics and Technology, Anhui Institute of Optics and Fine  
13 Mechanics, Chinese Academy of Sciences, Hefei, 230031, China

14 <sup>7</sup>Key Laboratory of Precision Scientific Instrumentation of Anhui Higher Education Institutes,  
15 University of Science and Technology of China, Hefei, 230026, China

16

17 \*Correspondence: Cheng Liu ([chliu81@ustc.edu.cn](mailto:chliu81@ustc.edu.cn))

18

19

20 **Abstract.**

21 Air quality forecasting plays a critical role in mitigating air pollution. However, current  
22 physics-based air pollution predictions encounter challenges in accuracy and spatiotemporal  
23 resolution due to limitations in the understanding of atmospheric physical mechanisms,  
24 observational constraints, and computational capacity. The world's first geostationary satellite  
25 UV-Vis spectrometer, i.e., the Geostationary Environment Monitoring Spectrometer (GEMS),  
26 offers hourly measurements of atmospheric trace gas pollutants at high spatial resolution over  
27 East Asia. In this study, we successfully incorporate Geostationary satellite observations into  
28 a neural network model (GeoNet) to forecast full-coverage surface nitrogen dioxide (NO<sub>2</sub>)  
29 concentrations over eastern China at 4-hour intervals for the next 24 hours. GeoNet leverages  
30 spatiotemporal series of satellite NO<sub>2</sub> observations to capture the intricate relationships among  
31 air quality, meteorology, and emissions in both temporal and spatial domains. Evaluation  
32 against ground-based measurements demonstrates that GeoNet accurately predicts diurnal  
33 variations and spatial distribution details of next-day NO<sub>2</sub> pollution, yielding the coefficient of  
34 determination of 0.68 and root mean square of error of 12.31  $\mu\text{g}/\text{m}^3$ , significantly surpassing  
35 traditional air quality model forecasts. The model's interpretability reveals that geostationary  
36 satellite observations notably improve NO<sub>2</sub> forecast capability more than other input features,  
37 especially over polluted regions. Our findings demonstrate the significant potential of  
38 geostationary satellite observations in artificial intelligence-based air quality forecasting, with  
39 implications for early warning of air pollution events and human health exposure.

40 **Keywords:** air quality forecast; deep learning; health impact; satellite remote sensing;  
41 nitrogen dioxide;

## 42 **1 Introduction**

43        Since the industrial revolution, numerous countries worldwide have encountered severe  
44 air pollution issues such as photochemical ozone smog and haze pollution (Hong et al., 2019),  
45 which significantly affect human health, crop yields, and the global environment (Guarin et al.,  
46 2024; Manisalidis et al., 2020; Sathe et al., 2021). Recent studies have shown that both long-  
47 term and short-term exposure to air pollutants such as nitrogen dioxide (NO<sub>2</sub>) can significantly  
48 affect human health, especially the respiratory system (Meng et al., 2021). Accurate and high  
49 spatial resolution predictions of air pollutant concentrations can provide critical information  
50 for sensitive persons to mitigate health risks. Meanwhile, air quality health risk (AQHI)  
51 forecasts and corresponding public response recommendations need to be communicated to the  
52 public promptly through public facilities (Fino et al., 2021; Tang et al., 2024). In recent decades,  
53 the advancement of atmospheric monitoring and modeling has enabled significant progress in  
54 air quality forecasting based on our understanding of atmospheric physics and chemistry  
55 (Peuch et al., 2022). Air pollution forecasting not only facilitates responses to environmental  
56 health risks but also improves the accuracy of climate and weather simulations (Makar et al.,  
57 2015). However, due to our still limited understanding of atmospheric mechanisms and  
58 observational and emission constraints, existing air quality forecasts based on physical or  
59 statistical models still face challenges in terms of temporal, spatial, and accuracy aspects  
60 (Campbell et al., 2022; Zhong et al., 2021).

61        Artificial Intelligence (AI) technology has made breakthroughs in the field of Earth  
62 science (Boukabara et al., 2020; Zhong et al., 2021), particularly excelling in addressing  
63 complex problems that are challenging for traditional physical paradigms to simulate (Irrgang  
64 et al., 2021), such as weather and climate forecasting (Andersson et al., 2021). Concerning  
65 meteorological data, some large-scale deep learning models have surpassed the predictive  
66 capabilities of existing numerical weather models to some extent, examples include Climax

67 (Nguyen et al., 2023), Pangu-Weather (Bi et al., 2023), and GraphCast (Lam et al., 2023).  
68 Despite significant progress and impressive performance achieved in meteorological variables  
69 forecasting with AI methods, there are still limitations in predicting atmospheric pollutant  
70 compositions. Compared to meteorological parameters, the prediction of air pollutant  
71 concentrations is affected by synoptic meteorology, chemistry, and anthropogenic emission  
72 activities, usually with more complex driven mechanisms and associated uncertainties. Current  
73 AI-based air quality forecasts often involve time series predictions at a limited number of  
74 observation stations, rather than full-coverage predictions over the entire spatial domain (Du  
75 et al., 2021). This is primarily due to the lack of effective air quality observations with high  
76 temporal and spatial resolution simultaneously.

77 While past polar-orbiting satellite observations such as the Ozone Monitoring Instrument  
78 (OMI) and the TROPospheric Monitoring Instrument (TROPOMI), have provided extensive  
79 coverage of atmospheric pollutant distributions such as nitrogen dioxide (NO<sub>2</sub>), sulfate dioxide  
80 (SO<sub>2</sub>), ozone (O<sub>3</sub>), and aerosols, they are limited to once-daily overpasses and usually affected  
81 by clouds (Chan et al., 2023; Van Geffen et al., 2022). This frequency usually exceeds the  
82 chemical lifetimes of many reactive gas pollutants like NO<sub>2</sub>, making it challenging to offer  
83 effective observational constraints for machine learning short-term air quality forecasting  
84 (Shah et al., 2020). However, these observations at a fixed daily overpass time could hardly  
85 support the prediction of atmospheric trace gas concentrations at other times of the day under  
86 different meteorological conditions. In February 2020, the world's first geostationary satellite  
87 payload for air pollution monitoring, the Geostationary Environment Monitoring Spectrometer  
88 (GEMS), began to provide high-coverage and high-precision air quality observations at an  
89 hourly rate for the East Asian region (J. Kim et al., 2020). The dynamic processes of air  
90 pollutants including emission, transformation, and transport can be observed by the  
91 geostationary satellite during the daytime. This monitoring capability may advance data-driven

92 air quality forecasting such as machine learning techniques by offering unprecedented  
93 observational constraints with high spatial and temporal coverage. Recent observing system  
94 simulation experiments (OSSE) indicate that assimilating trace gas observations by  
95 geostationary satellites into chemical models can effectively improve surface ozone  
96 simulations (Shu et al., 2023), nitrogen oxides (NO<sub>x</sub>), and emission estimates (Hsu et al., 2024).

97 Here, based on the unprecedented temporal and spatial resolution and coverage of the  
98 GEMS satellite (J. Kim et al., 2020), we incorporated Geostationary satellite remote sensing of  
99 tropospheric NO<sub>2</sub> column densities (refer to section 4 for details) into a neural Network model  
100 (GeoNet), to forecast full-coverage surface NO<sub>2</sub> concentration over the next day from the  
101 current time  $t$  (i.e.,  $t+24h$ ). Compared with previous air quality forecasting based on the  
102 simulation of atmospheric physics and chemistry possibly combined with data assimilation  
103 approaches, GeoNet relies solely on geostationary satellite measurements and ancillary  
104 meteorology data. GeoNet effectively addresses the complex nonlinear relationships between  
105 future short-term air quality and current satellite observations, as well as temporally adjacent  
106 meteorological variables (C. Zhang et al., 2022). The method employs satellite and  
107 meteorological variables within the spatial vicinity of individual air quality monitoring sites as  
108 input features, with site observations serving as labels for model training. The resulting model  
109 achieves accurate and comprehensive air quality predictions across the entire domain over East  
110 China, which is a significant achievement given that past machine learning technologies have  
111 relied on only a few stations or polar-orbiting satellite observations.

## 112 **2 Materials and Methods**

### 113 **2.1 Geostationary satellite observations of atmospheric NO<sub>2</sub>**

114 GEMS is the first UV-Vis spectrometer at a geostationary satellite orbit, measuring  
115 atmospheric pollutants such as NO<sub>2</sub>, SO<sub>2</sub>, O<sub>3</sub>, and HCHO over East Asia, at a spatial resolution  
116 of 3.5 km × 7.5 km at nadir and a temporal resolution of 1 hour during the daytime (J. Kim et

117 al., 2020). Based on the unique spectral absorption of trace gases, the atmospheric NO<sub>2</sub> column  
118 can be retrieved in visible wavelengths from the spectra of back-scattered sunlight. The details  
119 of the GEMS NO<sub>2</sub> retrieval can be found in the Algorithm Theoretical Basis Document  
120 (available at <https://nesc.nier.go.kr/ko/html/satellite/doc/doc.do>, last access: June 1, 2023). In  
121 this study, we used the tropospheric NO<sub>2</sub> column from the GEMS NO<sub>2</sub> version 2.0 product, as  
122 well as the cloud fraction for each satellite ground pixel. Overall, GEMS NO<sub>2</sub> measurements  
123 have a good correlation with ground-based remote sensing instruments, with correlation  
124 coefficients (R) between 0.69-0.81, and root mean square of errors (RMSE) between 3.2-  
125  $4.9 \times 10^{15}$  molecules/cm<sup>2</sup> (S. Kim et al., 2023). Our previous validation results indicated that  
126 GEMS NO<sub>2</sub> retrievals generally agreed well with ground-based MAX-DOAS measurements  
127 from 6 sites in China, with correlation coefficients ranging between 0.69-0.92 (Li et al., 2023).

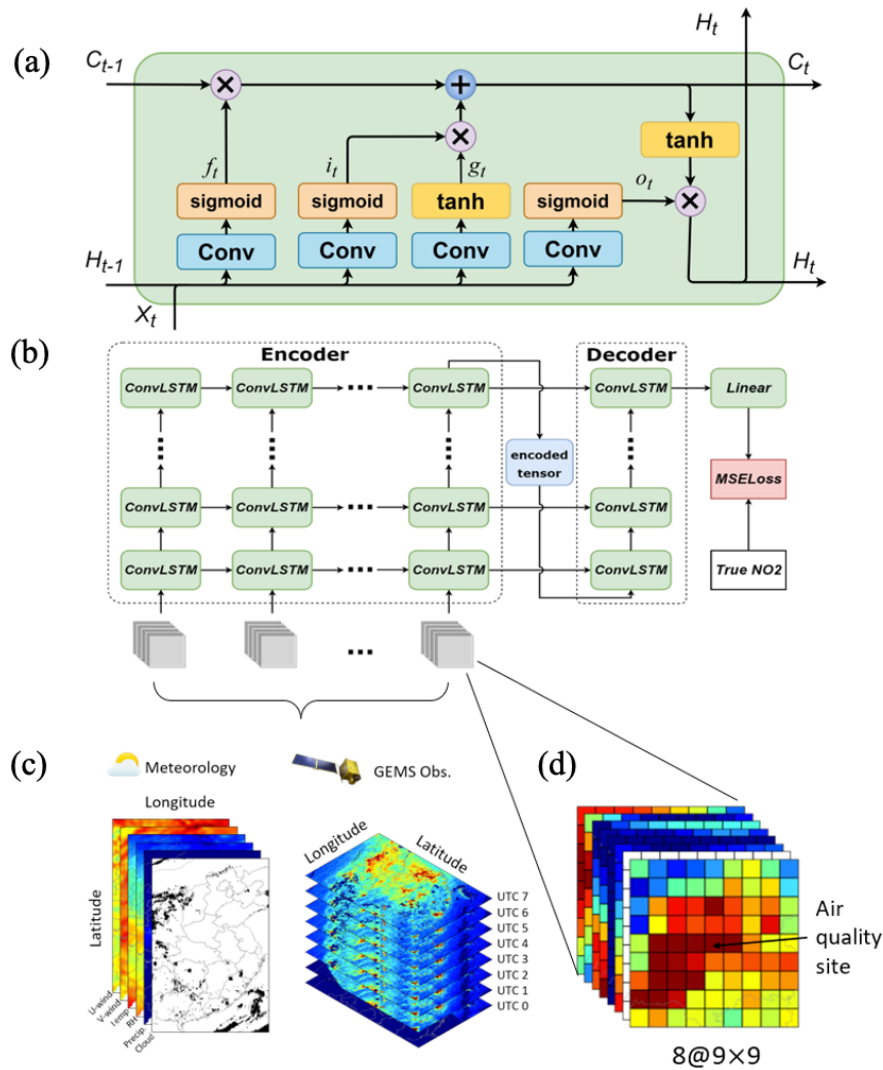
## 128 **2.2 Ancillary datasets**

129 Other input information including meteorological datasets is necessary to better constrain  
130 the prediction of future NO<sub>2</sub> pollution. Here, both the ERA5 meteorology reanalysis (Hersbach  
131 et al., 2020) and the CAMS forecast (Peuch et al., 2022) were used to provide meteorological  
132 parameters such as zonal and meridional wind (U-wind and V-wind), temperature (Temp),  
133 relative humidity (RH), and precipitation (Precip). In addition, the fraction of cloud cover  
134 available from the satellite NO<sub>2</sub> datasets was also considered. To fill the missing gaps in the  
135 satellite NO<sub>2</sub> measurements, we use both the NO<sub>2</sub> concentrations from the WRF-Chem model  
136 (C. Zhang et al., 2022) and the CAMS forecast of atmospheric composition. Note that the  
137 reanalysis datasets were typically updated with a week delay from real-time, while the forecast  
138 datasets can provide future 7-day meteorology from the current time. Therefore, the latency of  
139 input datasets would affect the operational prediction of the GeoNet model. Surface NO<sub>2</sub>  
140 measurements were used as the ground-truth label in the model training phase, available from

141 over 1000 national air quality sites by the China National Environmental Monitoring Centre  
 142 (CNEMC) (Kong et al., 2021).

143 The preprocessing steps of model input datasets, including outlier detection, missing value  
 144 handling, resampling, and normalization, are described in Supplementary Text S1.

145 **2.3 The GeoNet model**



146

147 **Figure 1.** The framework of predicting surface NO<sub>2</sub> map based on Geostationary satellite measurements and  
 148 a ConvLSTM neural network model (GeoNet). (a) the structure of the ConvLSTM block; (b) a diagram of  
 149 GeoNet model structure with inputs and output; (c) an illustration of the model input parameters including  
 150 meteorological variables and hourly NO<sub>2</sub> measurements by the Geostationary satellite; (d) the input data  
 151 cube of different features for single training batch, which is centered at an air quality site.

152 Fig. 1 illustrates the structure and methodology of the artificial intelligence air quality  
 153 forecasting model established in this study. Given the distinctive nature of spatiotemporal

154 sequence data for air quality, predictions must consider not only temporal relationships but also  
 155 spatial correlations. The deep learning model employed in this research utilizes convolutional  
 156 long short-term memory (ConvLSTM) as its kernel, a variant of the LSTM model designed for  
 157 the time series forecasting (Lin et al., 2020). It incorporates a convolutional network structure  
 158 to capture spatial features of three-dimensional inputs. Both input-to-state and state-to-state  
 159 transitions involve convolutional structures. ConvLSTM determines the future state of a unit  
 160 within a grid based on inputs from its local neighbors and past states, allowing it to effectively  
 161 model the spatiotemporal dynamics of air quality. The ConvLSTM kernel structure employed  
 162 in training is illustrated in Fig. 5a. Here,  $X_t$  represents the input at time  $t$ ,  $H_t$  and  $H_{t-1}$  denote  
 163 the outputs at times  $t$  and  $t-1$ , and  $C_t$  and  $C_{t-1}$  represent the states at times  $t$  and  $t-1$ . The  
 164 computational process is as follows:

$$165 \quad i_t = \sigma(X_t * w_{xi} + H_{t-1} * w_{hi} + b_i) \quad (1)$$

$$166 \quad f_t = \sigma(X_t * w_{xf} + H_{t-1} * w_{hf} + b_f) \quad (2)$$

$$167 \quad o_t = \sigma(X_t * w_{xo} + H_{t-1} * w_{ho} + b_o) \quad (3)$$

$$168 \quad g_t = \tanh(X_t * w_{xg} + H_{t-1} * w_{hg} + b_g) \quad (4)$$

$$169 \quad C_t = f_t \times C_{t-1} + i_t \times g_t \quad (5)$$

$$170 \quad H_t = o_t \times \tanh(C_t) \quad (6)$$

171 Where the asterisk (\*) represents the convolution operator,  $w$  is the convolution kernel,  $b$  is the  
 172 offset,  $\tanh$  is the hyperbolic tangent function, and  $\sigma$  is the activation function of Sigmoid.

173 The model primarily consists of three components: an encoder, a decoder, and fully  
 174 connected layers. Tropospheric NO<sub>2</sub> observations from the GEMS satellite for different  
 175 consecutive hours within a day, along with corresponding meteorological forecast field data,  
 176 serve as input features for model training. The encoder processes the spatiotemporal sequences  
 177 of input features for the preceding 8 hours ( $t-7h$ ,  $t-6h$ , ...,  $t$ ), which are then decoded by the  
 178 decoder. The final output, representing NO<sub>2</sub> concentrations at 4-hour intervals for the next 24



179 hours ( $t+4h$ ,  $t+8h$ ,  $t+12h$ , ...,  $t+24h$ ), is produced through fully connected layers. The loss  
180 function of mean squared error (MSE) is calculated by comparing the model output with the  
181 actual values from station observations, and the model undergoes iterative training. In the  
182 training task for a single station sample, the model utilizes continuous and distinct hourly  
183 dynamic images of all variables within the spatiotemporal vicinity of the station as input (see  
184 Fig. 1c-d). This effectively considers the intricate correlations in time and space between air  
185 quality, satellite observations, and meteorological input features. We train the GeoNet model  
186 with input features during the whole year of 2021. The training datasets were randomly selected  
187 from 75% of the whole samples, while the remaining 25% were used as validation sets.

#### 188 **2.4 The model configuration and optimization**

189 The model configurations and hyperparameters such as the optimizer, loss function, L1 or  
190 L2 regularization, dropout, training steps, and epochs can make a difference to the model  
191 performance including the prediction accuracy and generalizability. The performance metrics  
192 such as the coefficient of determination ( $R^2$ ), root mean square of error (RMSE), mean absolute  
193 error (MAE), and mean absolute percentage error (MAPE), were used to diagnose the model  
194 (see definition in Supplementary Text S2). Thus, several scenarios of model hyperparameters  
195 have been tested during the model training phase. The model accuracy on validation datasets  
196 and the learning rate curve were used to diagnose the model hyperparameters. The model  
197 parameters mainly include the number of layers and the dimensions of the hidden layers, both  
198 control the model's capacity. If the model capacity is relatively small, underfitting may occur;  
199 overfitting may exist if it is too large. Therefore, selecting an appropriate model capacity is  
200 crucial for improving model performance. During the pre-training process, the model is trained  
201 by combining different numbers of layers and dimensions of the hidden layers. The Mean  
202 Squared Error (MSE) Loss is recorded for each training iteration, and a heatmap is generated  
203 as shown in Fig. S2. From the heatmap, it can be observed that when the number of layers is 2

204 and the dimension of the hidden layer is 256, the model achieves the minimum MSE Loss. Fig.  
205 S3 shows the sensitivity test results of model loss varying with different batch size settings,  
206 indicating that a batch size of 64 is optimal. Based on the model's MSE loss under different  
207 hyperparameter configurations, the best-fitting model can be selected.

208 The Adam optimization algorithm controls the learning rate, which can design  
209 independent adaptive learning rates for different parameters. The three initialization parameters  
210  $\epsilon$ ,  $\rho_1$ , and  $\rho_2$  of the Adam algorithm are set to be 0.0001, 0.9, and 0.99, respectively. For the  
211 epoch, its size is controlled by the early stop method. The early stop method monitors the  
212 change of the model's loss function on the validation set during the training process and stops  
213 the model training immediately when the validation loss of the model starts to become larger.  
214 Due to the fluctuation of the loss function, a threshold  $p$  is set for the early stopping method in  
215 practice, and when the validation loss of the model becomes large for  $p$  consecutive epochs,  
216 the model is rolled back to the lowest validation loss and the training is stopped, and the  
217 threshold  $p$  is set to 10 in this paper. Fig. S4 shows a typical learning curve of the MSE loss in  
218 training and validation data sets for different learning steps in training an optimal model. Such  
219 diagnostics can be used to avoid the model overfitting.

## 220 **2.5 The importance of the model input feature**

221 Permutation feature importance is a technique used to assess the significance of each input  
222 feature in a machine-learning model (Altmann et al., 2010). The core idea is to evaluate the  
223 impact of each feature on model performance by randomly shuffling its values and observing  
224 the resulting change in the model's accuracy. In this study, for each input feature of the GeoNet,  
225 we iteratively shuffle its value independently while keeping other features unchanged, and then  
226 observe the model prediction on the modified input. The difference in the model prediction  
227 performance between using the original and shuffling input quantifies the feature's importance.  
228 Here, we measure the relative importance of each input feature using the metric of  $1-R^2$ , due

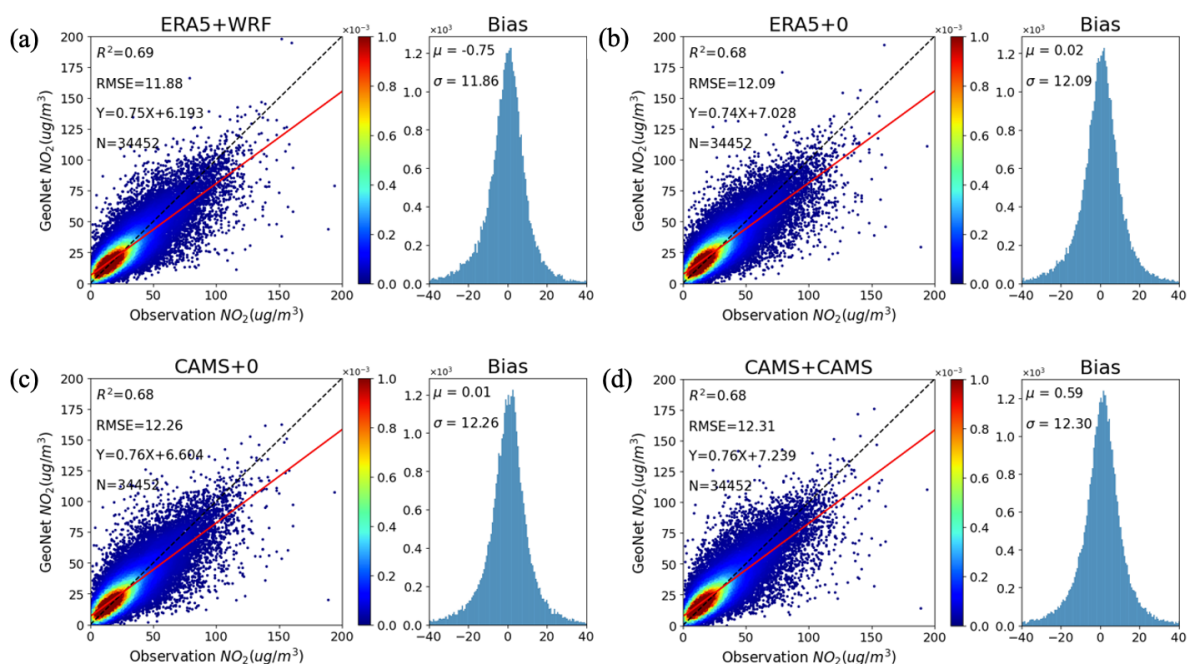
229 to its good standardized and indicative ability (C. Zhang et al., 2022). Generally, a larger  
230 performance drop indicates greater importance, as the model heavily relies on that feature for  
231 predictions. Conversely, smaller drops or increases suggest the feature may be less crucial or  
232 redundant. By permuting the input feature array based on the different spatial and temporal  
233 domains, we can gain a deeper understanding of how feature importance varies spatially and  
234 temporally. For example, the relative importance of one meteorology variable may vary with  
235 different diurnal, weekly, and monthly cycles, revealing the variability of its impact on the  
236 predicted NO<sub>2</sub> levels.

## 237 **3 Results and Discussion**

### 238 **3.1 Model performance**

239 Based on the GeoNet model and necessary input data (refer to section 2), we have  
240 achieved preliminary predictions of near-surface NO<sub>2</sub> concentration with full spatial coverage  
241 and a spatial resolution of 0.1 degrees over eastern China, at four-hour intervals over the next  
242 24 hours. In this study, we first tested the impact of using reanalysis and forecast meteorology  
243 datasets and filling in missing values in satellite observation data on the model predictions. The  
244 reanalysis datasets usually have higher precision than the forecast. Previous studies revealed  
245 that the accuracy of the information on meteorology and chemical composition significantly  
246 affects the performance of machine learning models in estimating air pollutant concentrations  
247 (Wang et al., 2024; Zuo et al., 2023). Due to the shielding effect of clouds, a considerable  
248 proportion of missing values may even exist in satellite NO<sub>2</sub> observations. Recent air quality  
249 big-data research usually requires the gap-filling of missing satellite data before inputting it  
250 into the machine learning model, either by spatial interpolation or regression techniques (M.  
251 Kim et al., 2021). We tested three methods for handling missing data, such as setting them to  
252 a fill value of zero, or replacing them by real-time CAMS simulated NO<sub>2</sub>, or WRF-Chem  
253 simulated NO<sub>2</sub> results (not real-time, but with higher precision).

254 The comparison results to the validation datasets indicate that the scenario using CAMS  
 255 meteorology datasets and replacing missing satellite NO<sub>2</sub> data with fill-values (Fig. 2c),  
 256 corresponds to a modest NO<sub>2</sub> prediction performance with  $R^2=0.68$  and  $RMSE=12.26 \mu\text{g}/\text{m}^3$ .  
 257 In contrast, the configuration scenario using ERA-5 reanalysis meteorology and imputing with  
 258 WRF-Chem simulations (Fig. 2a), corresponds to the best prediction performance of  $R^2=0.69$   
 259 and  $RMSE=11.88 \mu\text{g}/\text{m}^3$ . This may indicate that the importance of satellite missing data  
 260 imputation may be diminished by cloud mask inputs, especially since the model can extract  
 261 informative features from spatial and temporal neighboring inputs. To compromise between  
 262 the performance of real-time and accuracy, we selected the configuration scenario of using  
 263 CAMS meteorology and imputing with CAMS NO<sub>2</sub> (Fig. 2d) for subsequent discussion and  
 264 operational forecasting, with an  $R^2=0.68$  and  $RMSE=12.31 \mu\text{g}/\text{m}^3$ . In summary, the use of  
 265 higher-precision meteorology and filling missing NO<sub>2</sub> data enhances the model's prediction  
 266 accuracy on the validation dataset, but to a rather limited extent. This suggests that, unlike  
 267 previous machine learning techniques, GeoNet can effectively adapt to three-dimensional  
 268 inputs of varying accuracy and type, fully explore the spatiotemporal correlation of data  
 269 features, and demonstrate strong model generalization capabilities.



270

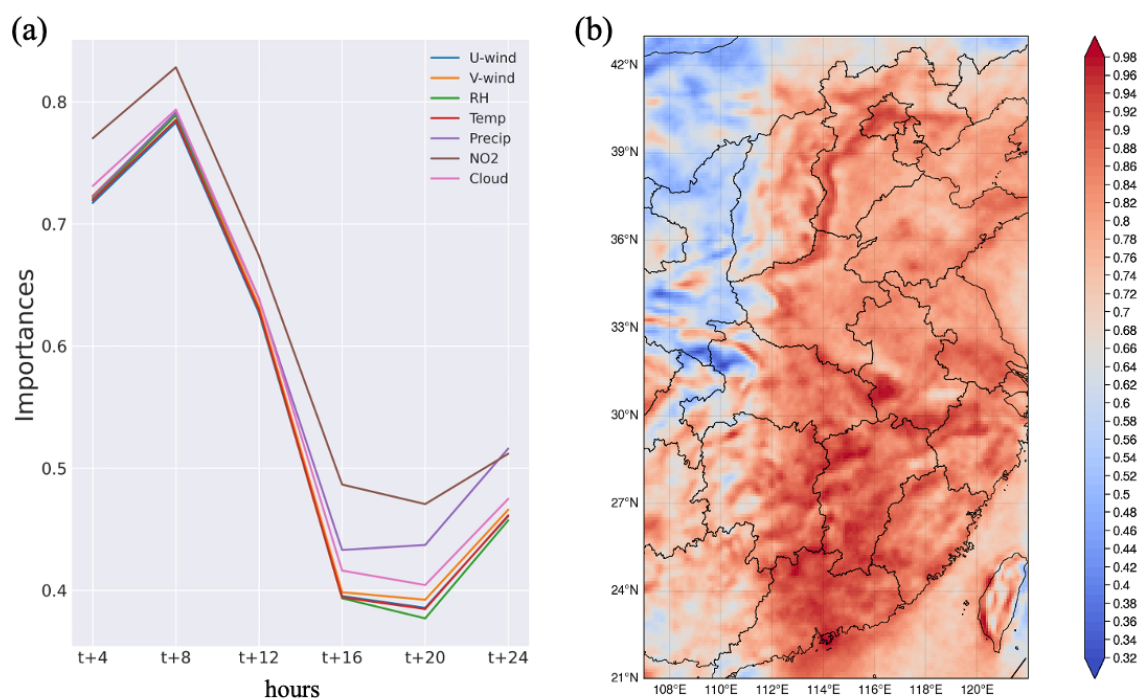
271 **Figure 2.** The GeoNet prediction performance of the surface NO<sub>2</sub> concentration compared to the validation  
272 samples, based on different input datasets of meteorology and atmospheric composition: (a) use ERA5  
273 meteorology and fill satellite measurement gaps with WRF-Chem simulated NO<sub>2</sub>; (b) use ERA5  
274 meteorology and NO<sub>2</sub> fill-value of zero for over gaps; (c) use CAMS meteorology and NO<sub>2</sub> fill-value of zero  
275 for gaps; (d) use CAMS meteorology and CAMS NO<sub>2</sub>. The left plot shows the scatter comparisons between  
276 GeoNet predictions and site observations, while the right plot shows the bias distribution between the two.

277 Figs. S5-S8 provide an overview of the major metrics (e.g., R<sup>2</sup>, RMSE, MAE, and MPE)  
278 of GeoNet prediction performance varying with prediction hours from t+4h to t+24h in  
279 different months. The results indicate that the model exhibits a higher correlation in NO<sub>2</sub>  
280 forecast during the spring and winter seasons compared to the summer, while the RMSE errors  
281 show the opposite trend. This could be attributed to much higher NO<sub>2</sub> pollution levels in winter  
282 months. Additionally, GeoNet's NO<sub>2</sub> prediction errors gradually increase during the next 24  
283 hours, particularly after t+20h. This is primarily due to the short lifetime of atmospheric NO<sub>2</sub>,  
284 leading to a diminishing constraint from historical observational data on future NO<sub>2</sub> predictions.  
285 Similar phenomena are also observed in machine learning or model-assisted weather forecasts  
286 (Andersson et al., 2021).

287 To assess the GeoNet model's performance for short-term pollution events, we compared  
288 it with near-surface NO<sub>2</sub> from CAMS forecasts, and in situ observations from CNEMC ground  
289 stations. Fig. S9 illustrates the daily time series of t+4h NO<sub>2</sub> from GeoNet, CAMS, and  
290 CNEMC for three typical sites in Beijing, Shanghai, and Guangzhou in 2021. As shown from  
291 the plot, NO<sub>2</sub> predictions by both GeoNet and CAMS generally agreed with the variation trends  
292 of CNEMC measurement. However, CAMS forecasts systematically overestimate the surface  
293 NO<sub>2</sub> concentration by 100%, possibly resulting from the biases in the NO<sub>x</sub> emission inventory  
294 (Douros et al., 2023). Compared to CAMS, the GeoNet prediction closely aligns with the  
295 ground-truth observations at CNEMC sites over eastern China, with an overall R<sup>2</sup> > 0.5 and  
296 mean bias < 5 μg/m<sup>3</sup> for polluted regions (see Fig. S10 and S11, respectively).

### 297 **3.2 Main factors in NO<sub>2</sub> forecast and their implications**

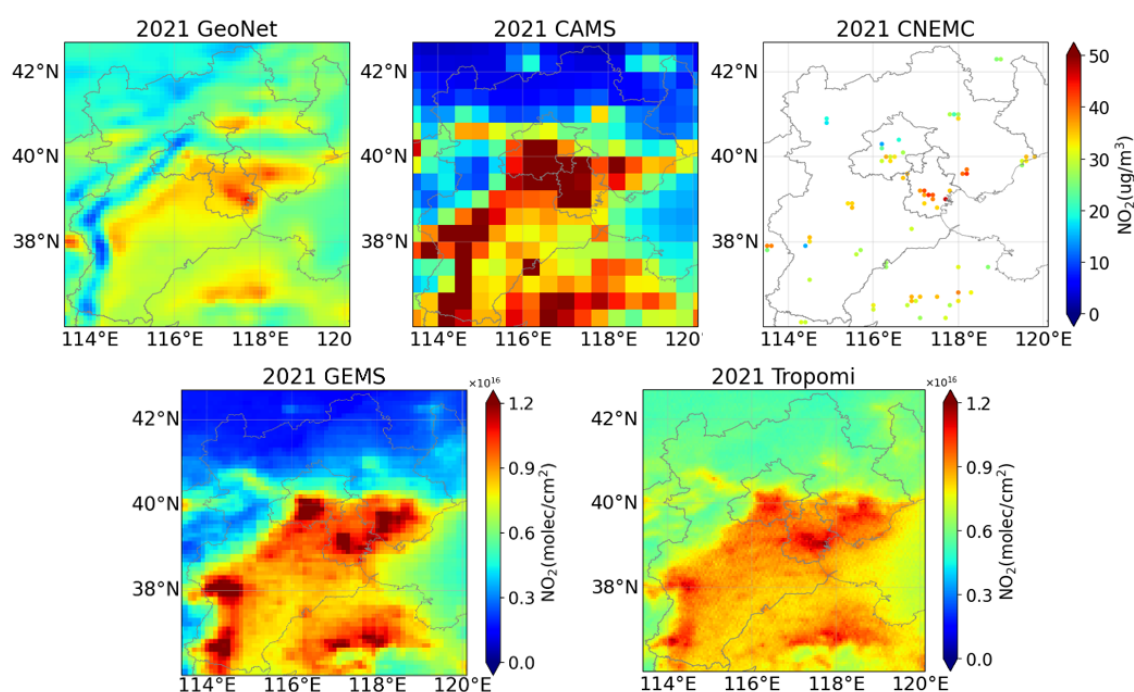
298 Previous physics-based numeric models of air quality prediction, e.g., the CAMS global  
 299 forecast model and the regional WRF-CMAQ model (Kuhn et al., 2024; Kumar et al., 2021;  
 300 Liu et al., 2023), can simulate the atmospheric physical and chemical processes (such as  
 301 advection, diffusion, deposition, and chemical reactions) by solving the atmospheric equations.  
 302 Recent data assimilation techniques further take real-time monitoring data from satellite and  
 303 ground-based platforms as model constraints to better predict air quality variables (Antje Inness  
 304 et al., 2022). Compared with physics-based models, “black-box” models such as the deep  
 305 learning technique usually lack interpretability and explainability (Q.-s. Zhang & Zhu, 2018).  
 306 This hinders the understanding and implications for predicting air quality variables such as  
 307 NO<sub>2</sub>. Here, we measure the relative importance of each input feature on the NO<sub>2</sub> forecast  
 308 accuracy, by iteratively permuting the input array and observing its influences on the model  
 309 prediction.



310  
 311 **Figure 3.** (a) The overall relative importance of different input features such as wind, surface pressure,  
 312 satellite NO<sub>2</sub>, and cloud mask, in GeoNet NO<sub>2</sub> forecast, varying with different hour steps from t+4h to t+24h.  
 313 (b) The spatial distribution of the relative importance of satellite NO<sub>2</sub> measurements in the GeoNet NO<sub>2</sub>  
 314 forecast in 2021.

315 Fig. 3a presents the relative importance ( $1-R^2$ ) of different input features varying with  
 316 prediction hour steps from t+4h to t+24h. The geostationary satellite NO<sub>2</sub> measurements play  
 317 the highest role in predicting surface NO<sub>2</sub> levels of the next day, although it degrades after t+8h.  
 318 Other meteorological input features also show a major impact on NO<sub>2</sub> prediction performance.  
 319 The significance of the different input variables remained generally consistent across seasons,  
 320 with minor variations (as shown in Fig. S12). By permutating the input array for each ground  
 321 pixel, Fig. 3b derived the spatial distribution of the relative importance of geostationary satellite  
 322 NO<sub>2</sub> in the predicting performance. Overall, satellite NO<sub>2</sub> has a higher impact in densely  
 323 populated areas experiencing severe air pollution, such as the Pearl River Delta, Yangtze River  
 324 Delta, and Jianghuai Plain, than in western China. Such results highlight the underappreciated  
 325 role of satellite NO<sub>2</sub> measurements with high spatial and temporal coverage in air pollution  
 326 forecasts.

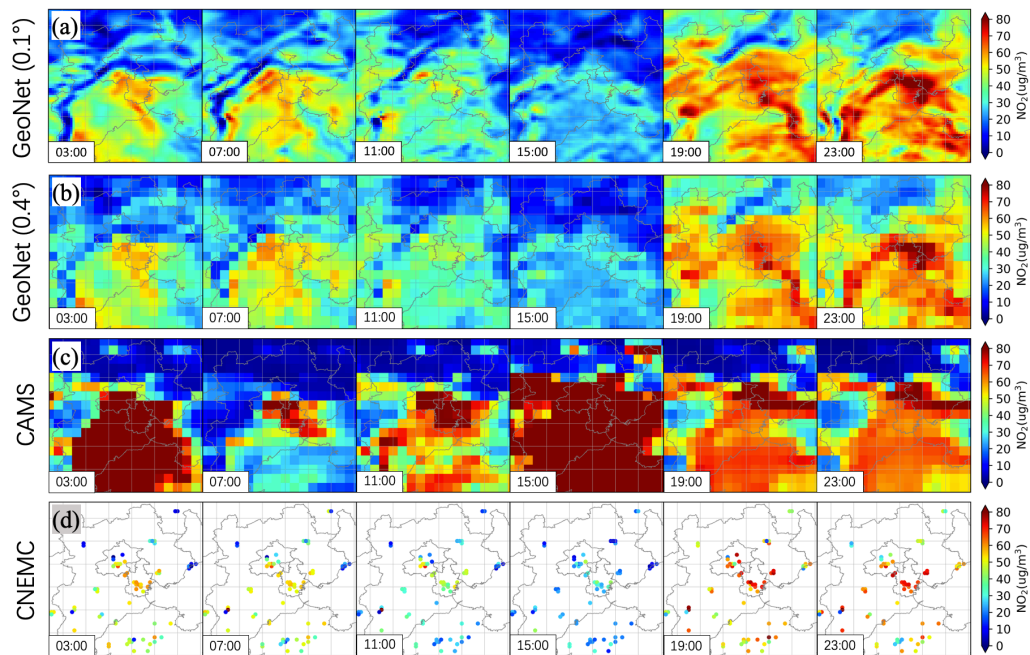
### 327 3.3 NO<sub>2</sub> pollution episodes and health exposure forecast



328 **Figure 4.** The comparisons of annual surface NO<sub>2</sub> concentrations from GeoNet, CAMS, and CNEMC,  
 329 respectively, (in the top panel), as well as the tropospheric NO<sub>2</sub> column observations from GEMS and  
 330 TROPOMI over East China in 2021 (in the bottom panel).  
 331

332 Beyond its prediction accuracy, GeoNet exhibits a pronounced advantage in spatial  
333 coverage and resolution, allowing for capturing finer-scale details in the pollutant distribution.  
334 Illustrated in Fig. 4, GeoNet demonstrates remarkable performance in predicting spatial  
335 nuances of NO<sub>2</sub> pollution, particularly when contrasted with ground-based and satellite  
336 observations. During a typical winter NO<sub>2</sub> pollution event (as shown in Fig. 5), GeoNet  
337 accurately simulates a significant decrease in concentrations at 11:00 and 15:00, probably led  
338 by intense photochemical activity in the daytime, coincident with ground-based observations.  
339 It also outperforms CAMS in predicting NO<sub>2</sub> variations throughout the day. The GeoNet model  
340 also retains the distributional differences in NO<sub>2</sub> concentrations between urban and rural areas,  
341 consistent with emission source characteristics and satellite observations. The suboptimal  
342 performance of CAMS predictions can be attributed to insufficient observational constraints  
343 and the use of outdated emission inventories (Douros et al., 2023). In the European region, the  
344 assimilation of TROPOMI observations into CAMS forecasts significantly improves the  
345 simulation accuracy of near-surface NO<sub>2</sub> concentrations and tropospheric column densities (A.  
346 Inness et al., 2019). Neural network methods, similar to GeoNet, could be used to correct and  
347 downscale forecast results by existing models (Baghanam et al., 2024). This approach holds  
348 promise for achieving operational air quality forecasts that balance efficiency and accuracy.



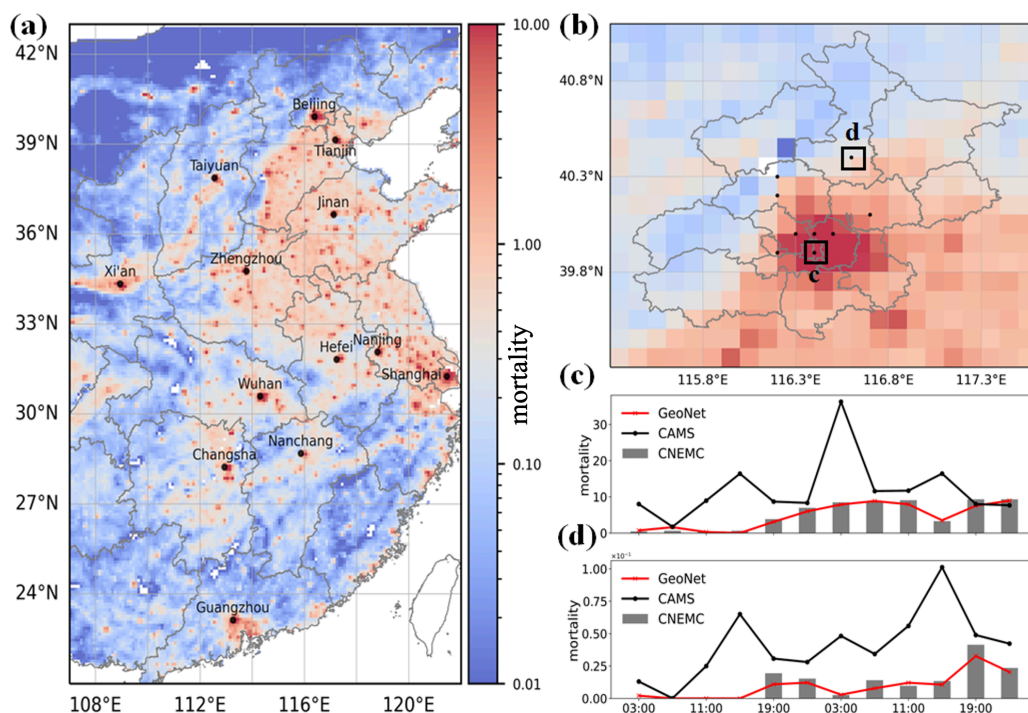


349

350 **Figure 5.** The spatial distribution comparisons of surface NO<sub>2</sub> concentration between (a) GeoNet prediction  
 351 at the original resolution of 0.1°, (b) GeoNet prediction resampled to the CAMS resolution of 0.4°, (c) CAMS  
 352 prediction, and (d) ground-based CNEMC site measurements. Note that the results are presented for different  
 353 continuing local hours (labeled text in the subplot) on 23 November 2021.

354 In this study, we used a simplified linearized risk model for the short-term NO<sub>2</sub> exposure  
 355 (Meng et al., 2021; C. Zhang et al., 2022) to calculate the distribution of all-cause mortality  
 356 risks based on GeoNet NO<sub>2</sub> predictions (see Fig. 6). Short-term NO<sub>2</sub> exposure leads to  
 357 remarkable regional differences in all-cause mortality, which are mainly concentrated in highly  
 358 polluted and densely populated urban areas. For both urban and suburban locations in Beijing  
 359 (see Fig. 6c-d), GeoNet-based NO<sub>2</sub> pollution exposure predictions are more consistent with  
 360 actual in situ observations than the CAMS forecasts. Current air quality health indices  
 361 forecasting based on limited station data has significant gaps, making it difficult to meet the  
 362 refined needs for different populations in urban, suburban, and rural areas. Integrating GeoNet  
 363 forecasts based on hourly geostationary satellite observations can support spatially  
 364 comprehensive and fine-scale air quality health risk prediction. This, in turn, guides managing

365 the risks of air pollution exposure-related diseases in sensitive populations and communities.



366

367 **Figure 6.** Mortality risk of short-term NO<sub>2</sub> exposure based on the GeoNet prediction on November 23, 2021.  
368 (a) mean mortality due to the predicted NO<sub>2</sub> exposure in East China; (b) a zoom-in map over Beijing and its  
369 neighboring area; (c) and (d) are comparisons of mortality estimation over the Beijing urban and rural  
370 regions (the rectangle areas presented in b), respectively, based on different NO<sub>2</sub> exposure prediction among  
371 GeoNet, CAMS, and CNEMC.

#### 372 4 Conclusion

373 The GeoNet model utilizes the unprecedented hourly air quality observations from  
374 geostationary satellites and resolves nonlinear associations in spatiotemporal proximity across  
375 multiple data sources. It achieves seamless short-term regional air quality predictions,  
376 exhibiting significant performance advantages over existing machine-learning air quality  
377 prediction models. To strike a balance between real-time and accuracy requirements, we  
378 evaluated the impact of using reanalysis- and forecast-based meteorology datasets, as well as  
379 imputing the missing values of satellite NO<sub>2</sub>. The findings reveal that the GeoNet model  
380 demonstrates robust generalization across diverse datasets, with minimal fluctuations in  
381 prediction performance. Overall, the model achieves an RMSE of 12.31  $\mu\text{g}/\text{m}^3$  and an  $R^2$  of  
382 0.68 in predicting NO<sub>2</sub> concentrations every 4 hours for the next 24 hours. However, validation

383 accuracy notably diminishes after t+16h within the next 24 hours, with stronger predictive  
384 correlations observed in seasons characterized by severe pollution, such as spring and winter,  
385 compared to summer. The variation of the model forecasting performance also shows that  
386 accurate prediction for longer time windows and heavy pollution events is still a major  
387 difficulty. This may be due to the high level of uncertainty in emissions and meteorology. In  
388 the future, a combination of higher resolution and more accurate multi-source data constraints,  
389 as well as machine learning models coupled with atmospheric physical mechanisms, may be  
390 needed to improve the existing forecasts.

391       Compared to traditional chemical model forecasts and data assimilation predictions, the  
392 GeoNet model handles various data sources, including meteorological simulations and air  
393 quality observations, and more accurately captures spatial intricacies of air pollution evolution.  
394 The GeoNet framework elucidated in this study forecasts short-term near-surface NO<sub>2</sub>  
395 concentrations and demonstrates transferable learning potentials for predicting other pollutants.  
396 This work also has important implications for the prediction of near-surface O<sub>3</sub> and particulate  
397 matter. For example, the integration of using vertical O<sub>3</sub> profiles from the GEMS satellite, in  
398 particular near-surface layer concentrations, and their joint observations of important O<sub>3</sub>  
399 precursors including NO<sub>2</sub> and HCHO, is expected to significantly improve the uncertainty of  
400 existing estimates of near-surface air pollution. This study underscores the pivotal role of next-  
401 generation stationary satellite observations of air pollution constituents in air quality  
402 forecasting, with the potential to advance operational air quality forecasting and mitigate  
403 associated health risks by integrating machine learning technologies.

404

405 **Data and code availability.** The GEMS NO<sub>2</sub> v2.0 data is available from the National Institute  
406 of Environmental Research (NIER) of South Korea (<https://nesc.nier.go.kr/en/html/index.do>,  
407 last access: December 10, 2023). We downloaded the NO<sub>2</sub> measurements from the CNEMC  
408 real-time air quality platform (<https://air.cnemc.cn:18007/>, last access: Jun 8, 2023). ERA-5  
409 reanalysis meteorological data is obtained from the European Center for Medium-Range  
410 Weather Forecasts (<https://climate.copernicus.eu/climate-reanalysis>, last access: December 8,  
411 2023). CAMS forecast of meteorological and atmospheric NO<sub>2</sub> datasets are retrieved from the  
412 CAMS Atmosphere Data Store (<https://ads.atmosphere.copernicus.eu/>, last access: December  
413 8, 2023). The source codes of the GeoNet model, surface NO<sub>2</sub> prediction, and necessary input  
414 data can be obtained from Chengxin Zhang ([zcx2011@ustc.edu.cn](mailto:zcx2011@ustc.edu.cn)) upon reasonable request.  
415

416 **Contributions:** C.Z. implemented the GeoNet model and analyzed the data. C.L. supervised  
417 the study. C.Z. wrote the manuscript with input from all co-authors.  
418

419 **Competing interests:** The contact author has declared that none of the authors has any  
420 competing interests.  
421

422 **Acknowledgments.** This study was supported by the National Natural Science Foundation of  
423 China (Nos. 42225504, 62305322, and 42375120), the National Key Research and  
424 Development Program of China (Nos. 2022YFC3700100 and 2023YFC3706104), the  
425 Fundamental Research Funds for the Central Universities (Nos. YD2090002021 and  
426 WK2090000038) and the New Cornerstone Science Foundation through the XPLOER  
427 PRIZE (2023-1033).  
428

## 429 **References**

- 430 Altmann, A., Tolosi, L., Sander, O., & Lengauer, T. (2010). Permutation importance: a  
431 corrected feature importance measure. *Bioinformatics*, 26(10), 1340-1347.  
432 <https://www.ncbi.nlm.nih.gov/pubmed/20385727>
- 433 Andersson, T. R., Hosking, J. S., Pérez-Ortiz, M., Paige, B., Elliott, A., Russell, C., et al.  
434 (2021). Seasonal Arctic sea ice forecasting with probabilistic deep learning. *Nature*  
435 *Communications*, 12(1), 5124.
- 436 Baghanam, A. H., Nourani, V., Bejani, M., Pournali, H., Kantoush, S. A., & Zhang, Y. (2024).  
437 A systematic review of predictor screening methods for downscaling of numerical  
438 climate models. *Earth-Science Reviews*, 104773.
- 439 Bi, K., Xie, L., Zhang, H., Chen, X., Gu, X., & Tian, Q. (2023). Accurate medium-range  
440 global weather forecasting with 3D neural networks. *Nature*, 1-6.
- 441 Boukabara, S.-A., Krasnopolsky, V., Penny, S. G., Stewart, J. Q., McGovern, A., Hall, D., et  
442 al. (2020). Outlook for exploiting artificial intelligence in the earth and environmental  
443 sciences. *Bulletin of the American Meteorological Society*, 1-53.
- 444 Campbell, P. C., Tang, Y., Lee, P., Baker, B., Tong, D., Saylor, R., et al. (2022).  
445 Development and evaluation of an advanced National Air Quality Forecasting  
446 Capability using the NOAA Global Forecast System version 16. *Geoscientific Model*  
447 *Development*, 15(8), 3281-3313.
- 448 Chan, K. L., Valks, P., Heue, K.-P., Lutz, R., Hedelt, P., Loyola, D., et al. (2023). Global  
449 Ozone Monitoring Experiment-2 (GOME-2) daily and monthly level-3 products of  
450 atmospheric trace gas columns. *Earth System Science Data*, 15(4), 1831-1870.
- 451 Douros, J., Eskes, H., van Geffen, J., Boersma, K. F., Compernelle, S., Pinardi, G., et al.  
452 (2023). Comparing Sentinel-5P TROPOMI NO<sub>2</sub> column observations with the

- 453 CAMS regional air quality ensemble. *Geoscientific Model Development*, 16(2), 509-  
454 534.
- 455 Du, S., Li, T., Yang, Y., & Horng, S. J. (2021). Deep Air Quality Forecasting Using Hybrid  
456 Deep Learning Framework. *IEEE Transactions on Knowledge and Data Engineering*,  
457 33(6), 2412-2424.
- 458 Fino, A., Vichi, F., Leonardi, C., & Mukhopadhyay, K. (2021). An overview of experiences  
459 made and tools used to inform the public on ambient air quality. *Atmosphere*, 12(11),  
460 1524.
- 461 Guarin, J. R., Jägermeyr, J., Ainsworth, E. A., Oliveira, F. A., Asseng, S., Boote, K., et al.  
462 (2024). Modeling the effects of tropospheric ozone on the growth and yield of global  
463 staple crops with DSSAT v4. 8.0. *Geoscientific Model Development*, 17(7), 2547-  
464 2567.
- 465 Hersbach, H., Bell, B., Berrisford, P., Hirahara, S., Horányi, A., Muñoz-Sabater, J., et al.  
466 (2020). The ERA5 global reanalysis. *Quarterly Journal of the Royal Meteorological  
467 Society*, 146(730), 1999-2049.  
468 <https://rmets.onlinelibrary.wiley.com/doi/abs/10.1002/qj.3803>
- 469 Hong, C., Zhang, Q., Zhang, Y., Davis, S. J., Tong, D., Zheng, Y., et al. (2019). Impacts of  
470 climate change on future air quality and human health in China. *Proceedings of the  
471 National Academy of Sciences*, 116(35), 17193-17200.
- 472 Hsu, C. H., Henze, D. K., Mizzi, A. P., González Abad, G., He, J., Harkins, C., et al. (2024).  
473 An Observing System Simulation Experiment Analysis of How Well Geostationary  
474 Satellite Trace-Gas Observations Constrain NO<sub>x</sub> Emissions in the US. *Journal of  
475 Geophysical Research: Atmospheres*, 129(2), e2023JD039323.
- 476 Inness, A., Aben, I., Ades, M., Borsdorff, T., Flemming, J., Jones, L., et al. (2022).  
477 Assimilation of S5P/TROPOMI carbon monoxide data with the global CAMS near-  
478 real-time system. *Atmospheric Chemistry and Physics*, 22(21), 14355-14376.
- 479 Inness, A., Flemming, J., Heue, K. P., Lerot, C., Loyola, D., Ribas, R., et al. (2019).  
480 Monitoring and assimilation tests with TROPOMI data in the CAMS system: near-  
481 real-time total column ozone. *Atmospheric Chemistry and Physics*, 19(6), 3939-3962.  
482 <Go to ISI>://WOS:000462793200001
- 483 Irrgang, C., Boers, N., Sonnewald, M., Barnes, E. A., Kadow, C., Staneva, J., & Saynisch-  
484 Wagner, J. (2021). Towards neural Earth system modelling by integrating artificial  
485 intelligence in Earth system science. *Nature Machine Intelligence*, 3(8), 667-674.
- 486 Kim, J., Jeong, U., Ahn, M.-H., Kim, J. H., Park, R. J., Lee, H., et al. (2020). New era of air  
487 quality monitoring from space: Geostationary Environment Monitoring Spectrometer  
488 (GEMS). *Bulletin of the American Meteorological Society*, 101(1), E1-E22.
- 489 Kim, M., Brunner, D., & Kuhlmann, G. (2021). Importance of satellite observations for high-  
490 resolution mapping of near-surface NO<sub>2</sub> by machine learning. *Remote Sensing of  
491 Environment*, 264, 112573. <Go to ISI>://WOS:000688451300002
- 492 Kim, S., Kim, D., Hong, H., Chang, L.-S., Lee, H., Kim, D.-R., et al. (2023). First-time  
493 comparison between NO<sub>2</sub> vertical columns from Geostationary Environmental  
494 Monitoring Spectrometer (GEMS) and Pandora measurements. *Atmospheric  
495 Measurement Techniques*, 16(16), 3959-3972.
- 496 Kong, L., Tang, X., Zhu, J., Wang, Z. F., Li, J. J., Wu, H. J., et al. (2021). A 6-year-long  
497 (2013-2018) high-resolution air quality reanalysis dataset in China based on the  
498 assimilation of surface observations from CNEMC. *Earth System Science Data*,  
499 13(2), 529-570. <Go to ISI>://WOS:000622997600001
- 500 Kuhn, L., Beirle, S., Kumar, V., Osipov, S., Pozzer, A., Bösch, T., et al. (2024). On the  
501 influence of vertical mixing, boundary layer schemes, and temporal emission profiles

502 on tropospheric NO<sub>2</sub> in WRF-Chem—comparisons to in situ, satellite, and MAX-  
503 DOAS observations. *Atmospheric Chemistry and Physics*, 24(1), 185-217.

504 Kumar, V., Remmers, J., Beirle, S., Fallmann, J., Kerkweg, A., Lelieveld, J., et al. (2021).  
505 Evaluation of the coupled high-resolution atmospheric chemistry model system  
506 MECO (n) using in situ and MAX-DOAS NO<sub>2</sub> measurements. *Atmospheric*  
507 *Measurement Techniques*, 14(7), 5241-5269.

508 Lam, R., Sanchez-Gonzalez, A., Willson, M., Wirnsberger, P., Fortunato, M., Alet, F., et al.  
509 (2023). Learning skillful medium-range global weather forecasting. *Science*,  
510 382(6677), 1416-1421.

511 Li, Y., Xing, C., Peng, H., Song, Y., Zhang, C., Xue, J., et al. (2023). Long-term observations  
512 of NO<sub>2</sub> using GEMS in China: Validations and regional transport. *Science of The*  
513 *Total Environment*, 904, 166762.

514 Lin, Z., Li, M., Zheng, Z., Cheng, Y., & Yuan, C. (2020). *Self-attention convlstm for*  
515 *spatiotemporal prediction*. Paper presented at the Proceedings of the AAAI  
516 conference on artificial intelligence.

517 Liu, C., Wu, C., Kang, X., Zhang, H., Fang, Q., Su, Y., et al. (2023). Evaluation of the  
518 prediction performance of air quality numerical forecast models in Shenzhen.  
519 *Atmospheric Environment*, 314, 120058.  
520 <https://www.sciencedirect.com/science/article/pii/S1352231023004843>

521 Makar, P., Gong, W., Milbrandt, J., Hogrefe, C., Zhang, Y., Curci, G., et al. (2015).  
522 Feedbacks between air pollution and weather, Part 1: Effects on weather. *Atmospheric*  
523 *Environment*, 115, 442-469.

524 Manisalidis, I., Stavropoulou, E., Stavropoulos, A., & Bezirtzoglou, E. (2020).  
525 Environmental and health impacts of air pollution: a review. *Frontiers in public*  
526 *health*, 14.

527 Meng, X., Liu, C., Chen, R., Sera, F., Vicedo-Cabrera, A. M., Milojevic, A., et al. (2021).  
528 Short term associations of ambient nitrogen dioxide with daily total, cardiovascular,  
529 and respiratory mortality: multilocation analysis in 398 cities. *bmj*, 372.

530 Nguyen, T., Brandstetter, J., Kapoor, A., Gupta, J. K., & Grover, A. (2023). ClimaX: A  
531 foundation model for weather and climate. *arXiv preprint arXiv:2301.10343*.

532 Peuch, V.-H., Engelen, R., Rixen, M., Dee, D., Flemming, J., Suttie, M., et al. (2022). The  
533 Copernicus Atmosphere Monitoring Service: From Research to Operations. *Bulletin*  
534 *of the American Meteorological Society*, 103(12), E2650-E2668.

535 Sathe, Y., Gupta, P., Bawase, M., Lamsal, L., Patadia, F., & Thipse, S. (2021). Surface and  
536 satellite observations of air pollution in India during COVID-19 lockdown:  
537 Implication to air quality. *Sustainable cities and society*, 66, 102688.

538 Shah, V., Jacob, D. J., Li, K., Silvern, R. F., Zhai, S., Liu, M., et al. (2020). Effect of  
539 changing NO<sub>x</sub> lifetime on the seasonality and long-term trends of satellite-observed  
540 tropospheric NO<sub>2</sub> columns over China. *Atmospheric Chemistry and Physics*, 20(3),  
541 1483-1495.

542 Shu, L., Zhu, L., Bak, J., Zoogman, P., Han, H., Liu, S., et al. (2023). Improving ozone  
543 simulations in Asia via multisource data assimilation: results from an observing  
544 system simulation experiment with GEMS geostationary satellite observations.  
545 *Atmospheric Chemistry and Physics*, 23(6), 3731-3748.

546 Tang, K. T. J., Lin, C., Wang, Z., Pang, S. W., Wong, T.-W., Yu, I. T. S., et al. (2024).  
547 Update of Air Quality Health Index (AQHI) and harmonization of health protection  
548 and climate mitigation. *Atmospheric Environment*, 326, 120473.

549 Van Geffen, J., Eskes, H., Compernelle, S., Pinardi, G., Verhoelst, T., Lambert, J.-C., et al.  
550 (2022). Sentinel-5P TROPOMI NO<sub>2</sub> retrieval: impact of version v2. 2 improvements

551 and comparisons with OMI and ground-based data. *Atmospheric Measurement*  
552 *Techniques*, 15(7), 2037-2060.

553 Wang, S., Zhang, M., Gao, Y., Wang, P., Fu, Q., & Zhang, H. (2024). Diagnosing drivers of  
554 PM 2.5 simulation biases in China from meteorology, chemical composition, and  
555 emission sources using an efficient machine learning method. *Geoscientific Model*  
556 *Development*, 17(9), 3617-3629.

557 Zhang, C., Liu, C., Li, B., Zhao, F., & Zhao, C. (2022). Spatiotemporal neural network for  
558 estimating surface NO2 concentrations over north China and their human health  
559 impact. *Environmental Pollution*, 119510.

560 Zhang, Q.-s., & Zhu, S.-C. (2018). Visual interpretability for deep learning: a survey.  
561 *Frontiers of Information Technology & Electronic Engineering*, 19(1), 27-39.

562 Zhong, S., Zhang, K., Bagheri, M., Burken, J. G., Gu, A., Li, B., et al. (2021). Machine  
563 learning: new ideas and tools in environmental science and engineering.  
564 *Environmental Science & Technology*, 55(19), 12741-12754.

565 Zuo, C., Chen, J., Zhang, Y., Jiang, Y., Liu, M., Liu, H., et al. (2023). Evaluation of four  
566 meteorological reanalysis datasets for satellite-based PM2. 5 retrieval over China.  
567 *Atmospheric Environment*, 305, 119795.

568

569